RESEARCH ARTICLE

NANO · MICRO small
www.small-journal.com

A pH-Sensitive Stretchable Zwitterionic Hydrogel with Bipolar Thermoelectricity

Ling-Chieh Lee, Kang-Ting Huang, Yen-Ting Lin, U-Ser Jeng, Chia-Hsin Wang, Shih-Huang Tung, Chun-Jen Huang, and Cheng-Liang Liu**

Amid growing interest in using body heat for electricity in wearables, creating stretchable devices poses a major challenge. Herein, a hydrogel composed of two core constituents, namely the negatively-charged 2-acrylamido-2-methylpropanesulfonic acid and the zwitterionic (ZI) sulfobetaine acrylamide, is engineered into a double-network hydrogel. This results in a significant enhancement in mechanical properties, with tensile stress and strain of up to 470.3 kPa and 106.6%, respectively. Moreover, the ZI nature of the polymer enables the fabrication of a device with polar thermoelectric properties by modulating the pH. Thus, the ionic Seebeck coefficient (S_i) of the ZI hydrogel ranges from −32.6 to 31.7 mV K^{-1} as the pH is varied from 1 to 14, giving substantial figure of merit (ZT_i) values of 3.8 and 3.6, respectively. Moreover, a prototype stretchable ionic thermoelectric supercapacitor incorporating the ZI hydrogel exhibits notable power densities of 1.8 and 0.9 mW m^{-2} at pH 1 and 14, respectively. Thus, the present work paves the way for the utilization of pH-sensitive, stretchable ZI hydrogels for thermoelectric applications, with a specific focus on harvesting low-grade waste heat within the temperature range of 25–40 °C.

1. Introduction

In response to global concerns regarding climate change, along with the growing demand for energy resources, the field of thermoelectric technology has emerged as a leading solution for sustainable development.[1] In particular, this technology offers a highly promising avenue for harnessing the vast reserves of low-grade heat energy (typically below 100 °C) that constitute nearly two-thirds of the world's waste heat.[2] A notable development in this field revolves around the utilization of electronic thermoelectric (e-TE) materials to construct thermoelectric generators (TEGs). These innovative devices operate as dynamic waste heat recovery systems by leveraging the principles of the Seebeck effect, wherein mobile charge carriers respond to temperature gradients, thereby facilitating electrical energy generation.[3] Nevertheless, pronounced challenges remain due to the inherently low Seebeck coefficient (S) values of the traditional inorganic-based TEGs, which typically fall within the range of a few mV K^{-1}, thus presenting a significant barrier to the achievement of efficient heat-to-electricity conversion. Meanwhile, additional challenges include limited flexibility, dependence on rare earth elements, and the need for high thermal gradients. Therefore, it is of utmost importance to overcome these obstacles in order to make the TEGs viable and applicable across a wide range of potential uses.[4]

A promising solution to the aforementioned challenges in the field of thermoelectric energy conversion is provided by the ionic thermoelectric generators (i-TEGs), which exploit the thermo-diffusion of ionic charge carriers in response to temperature gradients. Due to the disparate diffusion coefficients and, hence, mobilities of the constituent anions and cations, these tend to accumulate at either the hot or cold electrode in a phenomenon known as the Soret effect. Simultaneously, electrons move from the electrodes to the external circuit to counterbalance the charge disparities generated by the accumulated ions. This unique approach, which provides a Seebeck coefficient (referred to as the ionic Seebeck coefficient, S_i) one to three orders of magnitude larger than that of e-TE materials, presents opportunities to improve the efficiency and

L.-C. Lee, Y.-T. Lin, C.-L. Liu
Department of Materials Science and Engineering
National Taiwan University
Taipei 10617, Taiwan
E-mail: liucl@ntu.edu.tw

K.-T. Huang, C.-J. Huang
Department of Chemical and Materials Engineering
National Central University
Taoyuan 32001, Taiwan
E-mail: cjhuang@ncu.edu.tw

The ORCID identification number(s) for the author(s) of this article can be found under https://doi.org/10.1002/smll.202311811

U-S. Jeng, C.-H. Wang
National Synchrotron Radiation Research Center
Hsinchu 30076, Taiwan

S.-H. Tung
Institute of Polymer Science and Engineering
National Taiwan University
Taipei 10617, Taiwan

C.-L. Liu
Advanced Research Center for Green Materials Science and Technology
National Taiwan University
Taipei 10617, Taiwan

DOI: 10.1002/smll.202311811

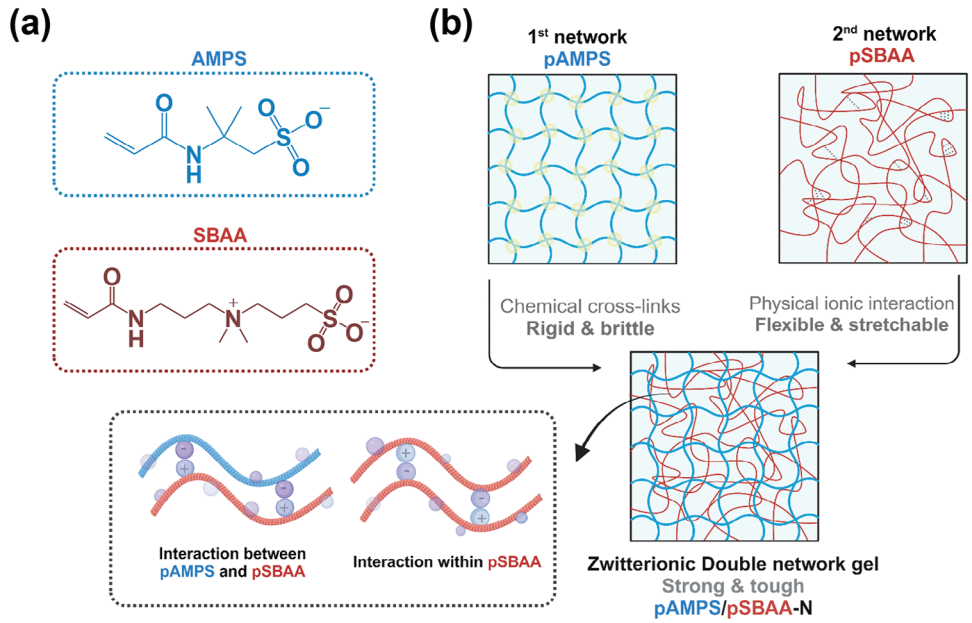

Figure 1. a) Molecular structures of the AMPS and SBAA monomers. b) Schematic representation depicting the first network, pAMPS hydrogels; the second network, pSBAA hydrogels; the zwitterionic double network hydrogel, pAMPS/pSBAA-N. The interactions between pAMPS and pSBAA and within pSBAA are also illustrated schematically.

practicality of thermoelectric technology. Thus, while the i-TE materials do not inherently generate electrons as the e-TE materials do, they possess a notable advantage in the form of supercapacitor-like characteristics, including the capacity to sustain a substantial voltage of more than 10 mV K^{-1}. This distinct feature opens up new avenues for the application of i-TE materials in practical energy storage and conversion systems.

An important determinant in achieving high-performance i-TE properties is the precise control of the cation or anion fractions within the polyelectrolyte.[3a,5] In this regard, considerable efforts have been directed toward exploiting either interactions between the ions and non-covalent bonds in the matrix (e.g., ion-dipole interactions) or ion-ion interactions between the anions and cations within the i-TE system. For example, Zhou et al. demonstrated the creation of an ionogel composed of 1-ethyl-3-methylimidazolium dicyanamide (EMIM:DCA) and poly(vinylidene fluoride-*co*-hexafluoropropylene) (PVDF-HFP) with cationic doping.[6] Because the strongly electron-withdrawing F-groups in the PVDF-HFP led to interactions between the matrix and ions, a sodium dicyanamide (Na-DCA) dopant was added to the ionogel to provide additional interactions between the matrix and the Na^+ cations and DCA^- anions of the dopant, thus resulting in an increased disparity between the mobilities of the $EMIM^+$ cations and the DCA^- anions. This resulted in a superior S_i value of 45 mV K^{-1} and a ZT_i value of 6.1 at a relative humidity (RH) of 85%. Meanwhile, Ho et al. reported the use of zwitterionic (ZI) polymers, which are characterized by an equal number of cations and anions along their polymer chains.[7] In that study, the positions of the positive and negative moieties in the polymer side chain were strategically adjusted to achieve effective control of the movement of free ions within the ionogel. This approach, involving unique binding interactions between ionic and polymer functional groups, led to the successful development of bipolar i-TE materials. Nevertheless, while extensive research efforts have focused on the introduction of additional materials or the use of diverse polymers to enhance the anion or cation mobility,[8] there has been comparatively little exploration into the use of pH-sensitive ZI polymers to achieve bipolar i-TE properties by adjusting the pH of the environment. This unexplored area of investigation holds considerable potential for advancing the present understanding of ion transport dynamics within polymer matrices. A summary of the bipolar thermoelectric properties of recently reported i-TE materials is provided in Table S1, Supporting Information. By leveraging pH manipulation to alter segment chargeability, specific ion mobility is enhanced, enabling the attainment of bipolar thermoelectric properties. When connecting p- and n-type i-TE materials in series to build TE modules, higher thermovoltage generation is achieved in practical applications, thereby increasing their applicability across diverse fields.

Hence, in the present work, a ZI polyelectrolyte based on the negatively charged 2-acrylamido-2-methylpropanesulfonic acid (AMPS) in combination with the ZI sulfobetaine acrylamide (SBAA) is synthesized via a two-step photopolymerization process (the chemical structure depicted in **Figure 1a**). The resulting double-network hydrogel, identified as pAMPS/pSBAA-N (with N indicating soaking in deionized water), demonstrates outstanding stretchability. To investigate the impact of pH, the hydrogels are submerged in aqueous solutions spanning pH values from ≈1 to 14. The resulting hydrogels are denoted as pAMPS/pSBAA-X, where X represents the specific pH value. Remarkably, pAMPS/pSBAA-1 and pAMPS/pSBAA-14 hydrogels each exhibit a substantial ionic conductivity (σ_i) of 60 mS cm^{-1}, along with ionic Seebeck coefficients (S_i) of −32.6 and 31.7 mV K^{-1}, and ZT_i values of 3.8 and 3.6, respectively. Finally, ionic thermoelectric supercapacitors (ITESCs) are

fabricated using the pAMPS/pSBAA-1 and pAMPS/pSBAA-14 hydrogels, and are shown to provide impressive power densities of 1.8 and 0.9 mW m^{-2}, respectively, under an external load resistance of 60 kΩ. This result demonstrates the versatile and promising nature of the as-developed ZI hydrogel for applications in ionic thermoelectric systems, offering noteworthy performance across a broad pH range.

2. Results and Discussion

The ZI polymer, which incorporates both positive and negative charges in the same side chain, exhibits enhanced hydrophilicity due to the higher density of cationic and anionic groups. However, this increased hydrophilicity results in poorer tensile stress.[9] Therefore, as shown schematically in Figure 1b and detailed in the Experimental Section, a two-step photopolymerization process was used to incorporate a pAMPS network with a high degree of chemical cross-linking (for enhanced tensile stress) along with a pSBAA ZI polymer to impart the hydrogel with flexible and stretchable properties via ionic interactions. Additionally, the interactions between the pAMPS and pSBAA, as well as interactions within the pSBAA itself, are expected to provide the ZI double-network with superior mechanical properties relative to those of other ZI system gels.[10] As shown schematically in Figure S1, Supporting Information, individual pAMPS and pSBAA hydrogels were prepared via the single-scaffold network photopolymerization of AMPS and SBAA, respectively, while the two-step photopolymerization process was performed to obtain the neutral pAMPS/pSBAA-N ZI double-network hydrogels. In the latter procedure, the pAMPS hydrogel was first fabricated by photopolymerization between two glass plates to form the first scaffold network. This was then immersed in a precursor solution comprising the SBAA monomer, *N,N'*-methylenebis(acrylamide) (MBAA) crosslinker, and 2-oxoglutaric acid (2-OA) initiator. During immersion, the notable swelling capacity of the pAMPS hydrogel facilitated the rapid diffusion of these precursors into the hydrogel, thus resulting in significant volumetric swelling. Subsequent UV irradiation then leads to the formation of a pSBAA network within the pre-existing pAMPS network. The successful fabrication of the pAMPS/pSBAA-N hydrogel is demonstrated by the Fourier transform infrared (FTIR) spectra in Figure S2, Supporting Information. Here, the pAMPS/pSBAA-N spectrum exhibits peaks at 1030 and 1486 cm^{-1} corresponding to the sulfonic acid (SO_3^-) and quaternary ammonium (N^+R_4) groups, respectively. Meanwhile, the FTIR spectrum of the single pAMPS hydrogel exhibits peaks at 1486 cm^{-1} corresponding to the N^+R_4, and that of the single pSBAA hydrogel exhibits peaks at 1030 and 1486 cm^{-1} corresponding to the SO_3^- and N^+R_4 groups, respectively.[10b,11]

In addition, the microstructural morphologies of the pAMPS/pSBAA-N hydrogels are revealed by the scanning electron microscope (SEM) images in **Figure 2**, while the microstructures of the single pAMPS and pSBAA hydrogels are shown in Figure 2a–d. Thus, the single pAMPS hydrogel exhibits interconnected porous scaffold structures, with an average pore size of ≈20 µm. This can be attributed to chemical cross-linking within the single network and can be expected to increase the mechanical brittleness and rigidity of the hydrogel structure.[12] By contrast, the single pSBAA hydrogel (Figure 2c,d) exhibits a more robust aggregation of polymer chains, with a larger average pore size of around 100 µm, due to the strong ionic interactions between the ZI polymer chains. As a result, the ZI hydrogel is expected to exhibit greater ductility, flexibility, and stretchability.[13] Meanwhile, as shown in Figure 2e,f, the pAMPS/pSBAA-N hydrogel combines the distinct properties of the two individual polymers to provide a denser structure with only a limited number of pores. Moreover, the presence of wrinkle structures indicates molecular entanglement between the pAMPS and pSBAA chains. This densely packed structural arrangement is expected to play a crucial role in providing the as-fabricated material with outstanding mechanical properties. Previous studies have suggested[14] that the dense microstructure observed in double-network hydrogels can significantly influence ion transport. The close packing of polymer chains and intermolecular interactions within the hydrogel matrix may enhance ion vibrational dynamics, thereby facilitating more efficient ion transport.

The mechanical properties of the stretchable pAMPS/pSBAA-N hydrogel are demonstrated in **Figure 3a**, where the ability of the material to undergo stretching, bending, knotting, and adhesion is shown photographically. As a further demonstration, the thermal rheological properties of the pAMPS/pSBAA-N and single pSBAA hydrogels are shown in Figure S3, Supporting Information. Here, the dynamic storage modulus (G') of each hydrogel is consistently larger than its loss modulus (G'') throughout the temperature range of 20–50 °C, thereby indicating that both hydrogels exhibit a stable quasi-solid behavior, rather than transforming to a liquid-like state, in response to temperature fluctuations.[15] It should also be noted that the G' values of the pAMPS/pSBAA-N hydrogel exceed those of the pSBAA hydrogel at each temperature, thereby confirming the enhanced tensile properties of the ZI double-network hydrogel. The mechanical response of the pAMPS/pSBAA hydrogels to varying pH environments is revealed by the stress–strain curves in Figure 3b,c. Here, the pAMPS/pSBAA-N hydrogel exhibits a high tensile strength of 470.3 kPa, along with an elongation of 106.6% at the breaking point. However, when the pH is either increased or decreased, the tensile strength decreases, while the elongation at the breaking point increases. Thus, after immersion in an acidic solution (pH 1), a tensile stress of 167.4 kPa and a breaking elongation of 157% are obtained, while immersion at pH 14 leads to a tensile stress of 228.3 kPa and a breaking elongation of 156%. The mechanisms behind these variations in tensile strength and breaking elongation are shown schematically in Figure 3d. Thus, immersion of the hydrogel in solutions of pH 1 or 14 disrupts the ionic interactions, as both cations (Na^+ and H^+) and anions (OH^- and Cl^-) interfere with the ionic bonding, thereby resulting in the relaxation of the polymer chains.[16] As a result, the mechanical properties of the hydrogels are significantly affected by altering the pH.

The impact of different temperatures (25–35 °C) on the nanostructure of the pAMPS/pSBAA-N hydrogel, as well as pAMPS/pSBAA-1 and pAMPS/pSBAA-14, is elucidated through small-angle X-ray scattering (SAXS) scattering curves and the corresponding fitting outcomes are presented in **Figure 4a** and Figure S4, Supporting Information. The numerical findings are summarized in **Table 1**. In this technique, the Beaucage unified

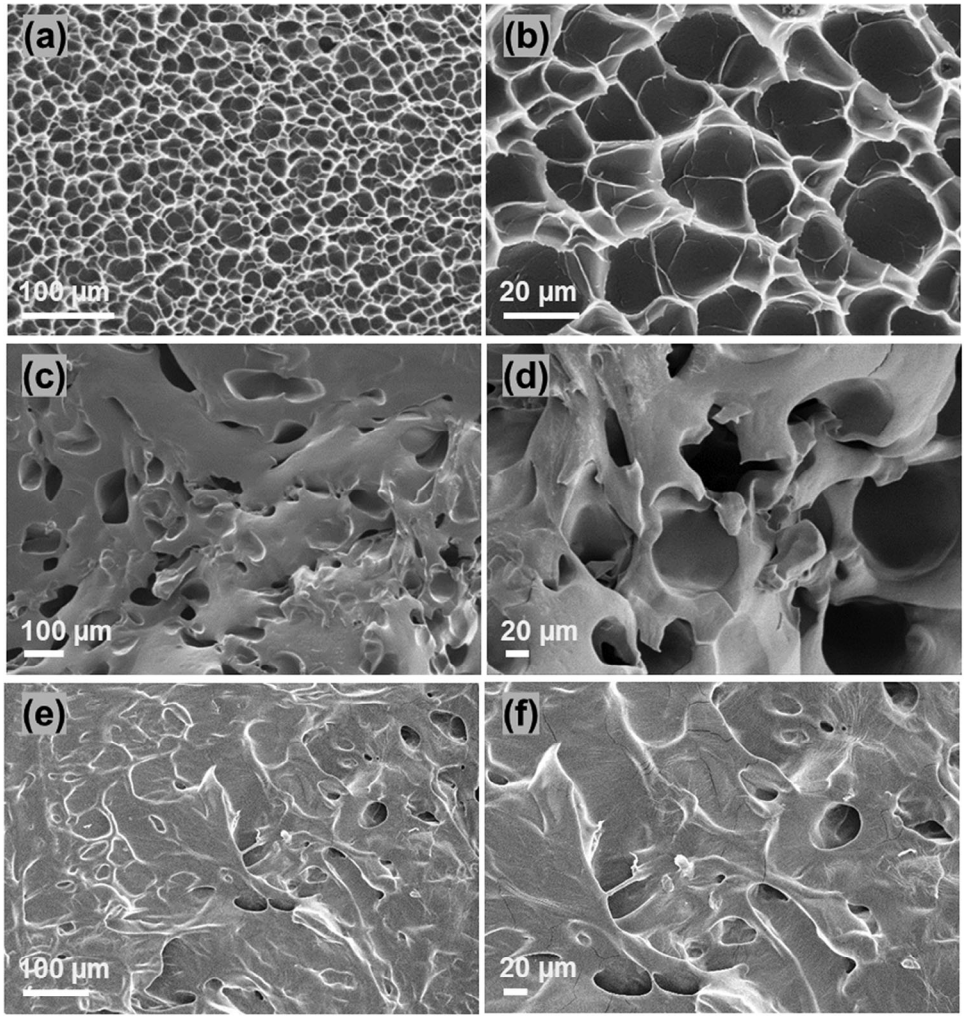

Figure 2. Cross-sectional SEM images of the lyophilized hydrogels: a) Microstructure of the pAMPS hydrogels and b) higher magnification detail of the pAMPS hydrogels. c) Microstructure of the pSBAA hydrogels and d) higher magnification detail of the pSBAA hydrogels. e) Microstructure of the pAMPS/pSBAA-N hydrogels and f) higher magnification detail of the pAMPS/pSBAA-N hydrogels.

equation is used to provide a versatile framework for modeling the scattering behaviors of a wide range of polymer structures including random coils, semi-flexible polymers, and various types of aggregates.[17] Furthermore, this approach allows for the in-depth characterization of the multi-level structure of the hydrogels and the various degrees of aggregation within the material by describing the number of unrestricted and interdependent structural levels therein. Thus, the Beaucage equation is presented here as Equation (1)

$$I(q) \cong I_{bkg} + \sum_{i=1}^{N} \left\{ G_i \exp\left(-\frac{q^2 R_{gi}^2}{3}\right) + B_i \exp\left(-\frac{q^2 R_{g(i+1)}^2}{3}\right) \times \left\{ \frac{\left[erf\left(\frac{qR_{gi}}{\sqrt{6}}\right)\right]^3}{q} \right\}^{P_i} \right\} \quad (1)$$

where G_i is the Guinier pre-exponential factor, B_i is the power law pre-exponential factor, R_{gi} is the radius of gyration, P_i is the fractal dimension, and the subscript i is associated with different levels of structural organization. Thus, $i = 1$ corresponds to the global structure, while $i = 2$ and $i = 3$ indicate local structures. Note that B_i is a constant prefactor specific to the type of power-law scattering observed as determined by the regime in which P_i falls which is dependent on the specific type of stepped law observed in a given section of the scattering curve.

Table 1. Fitting parameters of the three-level Beaucage Model applied to SAXS data extracted from hydrogel samples.

Sample	R_{g1}	P_1	R_{g2}	P_2	R_{g3}	P_3
	[Å]	[–]	[Å]	[–]	[Å]	[–]
pAMPS/pSBAA-N at 25 °C	1176	4	90	2	6.8	1
pAMPS/pSBAA-N at 30 °C	1041	4	72	2	6.4	1
pAMPS/pSBAA-N at 35 °C	1030	4	70	2	6.4	1
pAMPS/pSBAA-1[a)]	823	4	70	2	5.5	1
pAMPS/pSBAA-14[a)]	862	4	57	2	6	1.5

[a)] At 25 °C.

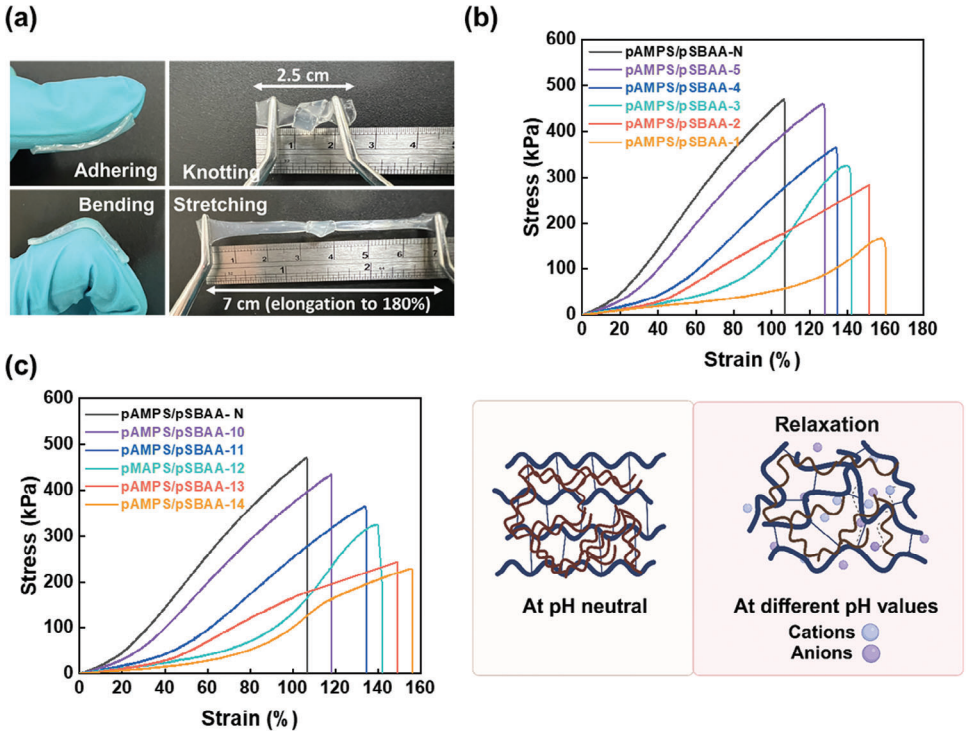

Figure 3. a) Photographic depiction of pAMPS/pSBAA-N hydrogel under different conditions: stretching, bending, knotting, and adhering. b) Tensile stress–strain curve under pH 1 to 5 conditions for pAMPS/pSBAA-X hydrogels. c) Tensile stress–strain curve under pH 10 to 14 conditions for pAMPS/pSBAA-X hydrogels. d) Schematics elucidating the interactions within the pAMPS/pSBAA-X polymer matrix involving cations and anions. The immersion in the varying pH solutions leads to the disruption of the ionic interactions, as both cations (Na^+ or H^+) and anions (OH^- or Cl^-) interfere with the established ionic bonding.

Thus, the unified fitting approach reveals the following three structural levels: 1) aggregates (q = 0.002–0.004 Å^{-1}), 2) clusters (q = 0.01–0.08 Å^{-1}), and 3) the primary structure of the polymer chains (q > 0.1 Å^{-1}). Remarkably, the same type of scattering curve is observed for the double-network hydrogel under all conditions of temperature and pH, with the power law fit indicating the following three fractal dimension regimes: i) $P_1 = 4$ in level 1, indicating a rougher fractal-like surface, ii) $P_2 = 2$ in level 2, which suggests that the building blocks assume the form of Gaussian coils, and iii) $P_3 = 1$ in level 3, thereby indicating that the primary structure consists of rod-like monomers.[18] However, the radii of gyration are not the same under all conditions. For instance, the Guinier fitting of the pAMPS/pSBAA-N hydrogel at 25 °C gives R_{g1} = 1176 Å for the aggregates (level 1), R_{g2} = 90 Å for the clusters (level 2), and R_{g3} = 6.8 Å for the primary polymeric structure (level 3). The R_{g1} and R_{g2} values under other conditions of temperature and pH are discussed in later paragraphs. Meanwhile, taking the power law and Guinier fitting results together, the three-level structure of the pAMPS/pSBAA-N hydrogel at 25 °C can be explained as shown schematically in Figure 4b. Thus, at level 3, the polymer segments adopt a rod-like structure, potentially indicating the presence of a crosslinked network.[19] At level 2, however, the building blocks can be envisioned as blobs containing the polymer chains, while, at level 1, the global network structure arises from the interconnection of these blobs via polymer aggregation.

However, while the same structural levels are observed when the temperature is increased from 25 to 30 and 35 °C, the R_{g1} value decreases from 1176 to 1041 and 1030 Å, respectively (Table 1). Similarly, the R_{g2} value decreases from 90 to 72 and 70 Å, respectively, with the same increase in temperature. This can be attributed to the thermosensitive nature of the ZI polymer, as indicated by the presence of an upper critical solution temperature (UCST) within its phase diagram.[20] Thus, at temperatures below the UCST, the ZI polymer adopts a contracted state, thereby leading to the formation of large, dense aggregates. As the temperature rises above the UCST, however, the polymer undergoes a higher degree of swelling due to the diffusion of more water, which in turn causes the aggregates to disperse into smaller particles. Meanwhile, at a fixed temperature of 25 °C, the R_{g1} decreases from 1176 Å at neutral to 823 and 862 Å at pH 1 and 14, respectively. Similarly, the R_{g2} value decreases from 90 Å at neutral to 70 and 57 Å at pH 1 and 14, respectively, at the same temperature. This can be attributed to the chaotropic natures of the various pH environments, such that the introduced ions (H^+ or OH^-) might disrupt the intermolecular interactions within the aggregates, thus resulting in the reduction of both the R_{g1} and R_{g2}.[21] This interpretation is consistent with the above analysis of the mechanical properties and explains the differential swelling behavior of the hydrogel according to the pH. Notably, the variation in R_{g1} and R_{g2} according to the pH of the environment is more substantial than the variation according to temperature.

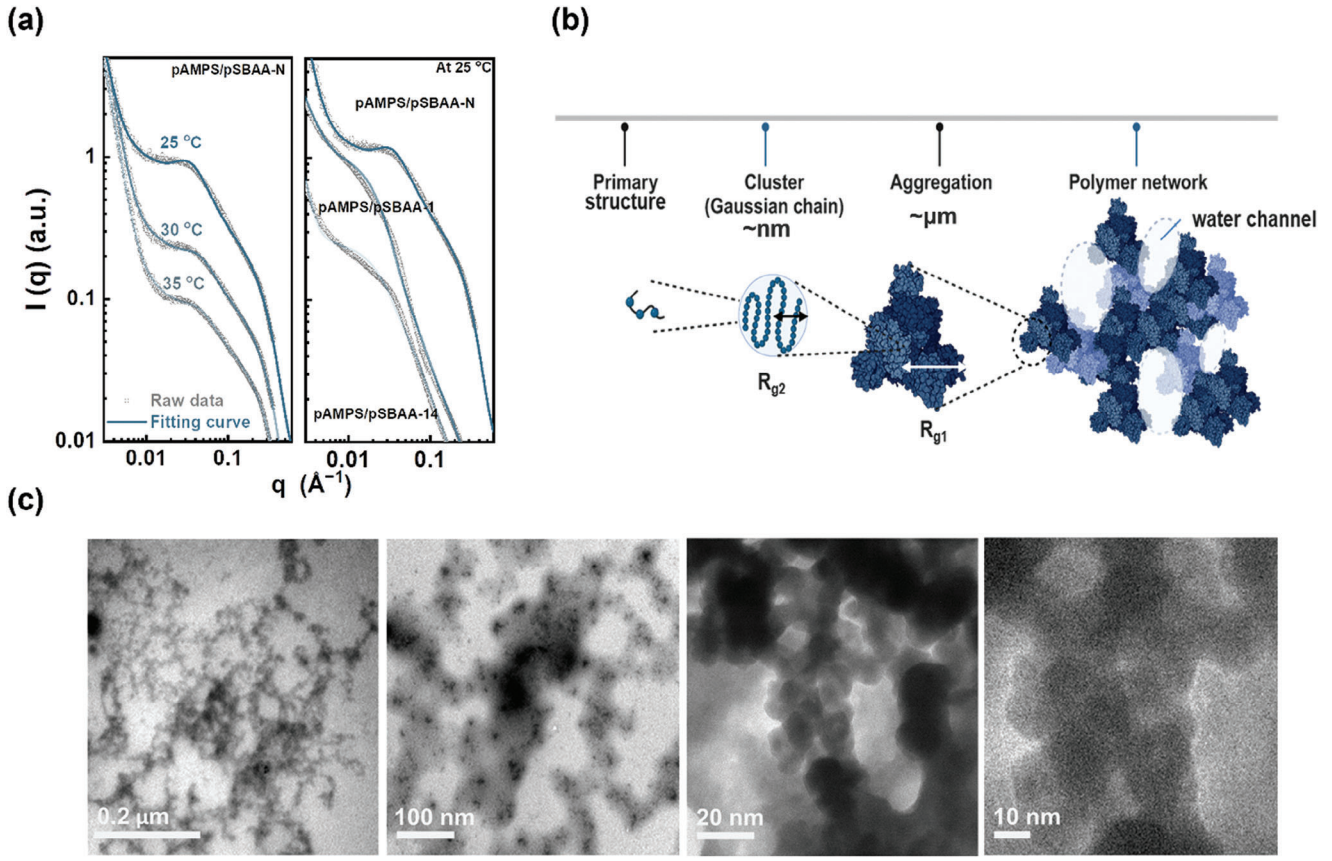

Figure 4. a) SAXS patterns of the pAMPS/pSBAA-N hydrogels under varying temperatures, along with pAMPS/pSBAA-1 and pAMPS/pSBAA-14 hydrogels at 25 °C. b) Schematic diagram portraying the nanostructure of pAMPS/pSBAA-N hydrogel according to the Beaucage Model, illustrating cluster formation through polymer chain aggregation via local segmental association. c) TEM images of pAMPS/pSBAA-N at different magnifications.

The above SAXS results are supported by the transmission electron microscope (TEM) images in Figure 4c.[22] Here, the low-magnification image reveals the fractal surface of the pAMPS/pSBAA-N at 25 °C, while the higher-magnification image reveals the clusters that form the fractal aggregates. Notably, both SAXS and TEM analyses indicate a particle size of around 90 Å. Hence, the TEM analysis confirms the accuracy of the SAXS fit results. Thus, the SAXS analysis of the pAMPS/pSBAA-N hydrogel has revealed a three-level hierarchical structure characterized by distinct power-law behaviors. The combination of TEM and SAXS has enabled the precise determination of the structural components of the hydrogel, including surface fractal aggregates and coil-like clusters, each supported by their respective power law exponents and radii of gyration, except for the rod-like monomers, which the instrument is restricted from measuring. Moreover, the observed decrease in R_{g1} and R_{g2} with increasing temperature demonstrates the inherent thermosensitive properties of the ZI polymers, while the variation in R_{g1} and R_{g2} according to the pH of the environment indicates that the chaotropic effect exerts a more substantial impact. Hence, the SAXS results underscore the pH sensitivity of the pAMPS/pSBAA-X hydrogels, thereby contributing to a more comprehensive understanding of the hydrogel structures.

The thermoelectric properties of the as-fabricated ZI hydrogel electrolyte under varying pH environments are revealed in **Figure 5**. The ionic Seebeck coefficient (S_i) values of the hydrogels were evaluated in the vertical direction by using a customized experimental setup. In this configuration, a controlled temperature gradient (ΔT) was applied to the two ends of the hydrogel, thereby generating a thermovoltage (ΔV). The S_i was then determined from the slope of the linear relationship between ΔV and ΔT in Equation (2)

$$s_i = -\frac{\Delta V}{\Delta T} = -\frac{V(T_H) - V(T_C)}{T_H - T_C} \quad (2)$$

where $V(T_H)$ is the voltage of the hot electrode at temperature T_H, and $V(T_C)$ is the voltage of the cold electrode at temperature T_C. Thus, in Figure 5a, negative S_i values are observed within the pH range of 1 to 3, with a maximum value of −32.6 mV K^{-1} at pH 1, thereby indicating n-type behavior. At pH values of 4 and 5, however, positive S_i values are observed, thereby indicating p-type behavior.[5h] Moreover, the p-type properties are seen to continue with the further increase in pH, reaching a maximum S_i value of +31.7 mV K^{-1} at pH 14. Thus, a point of transition is observed at pH = 4. The temporary change of ΔV from pAMPS/pSBAA-1 and pAMPS/pSBAA-14 hydrogels with supplied temperature differences is presented in Figure S5, Supporting Information. The linear fittings of the ΔV versus ΔT curves for the pAMPS/pSBAA-N are shown in Figure S6,

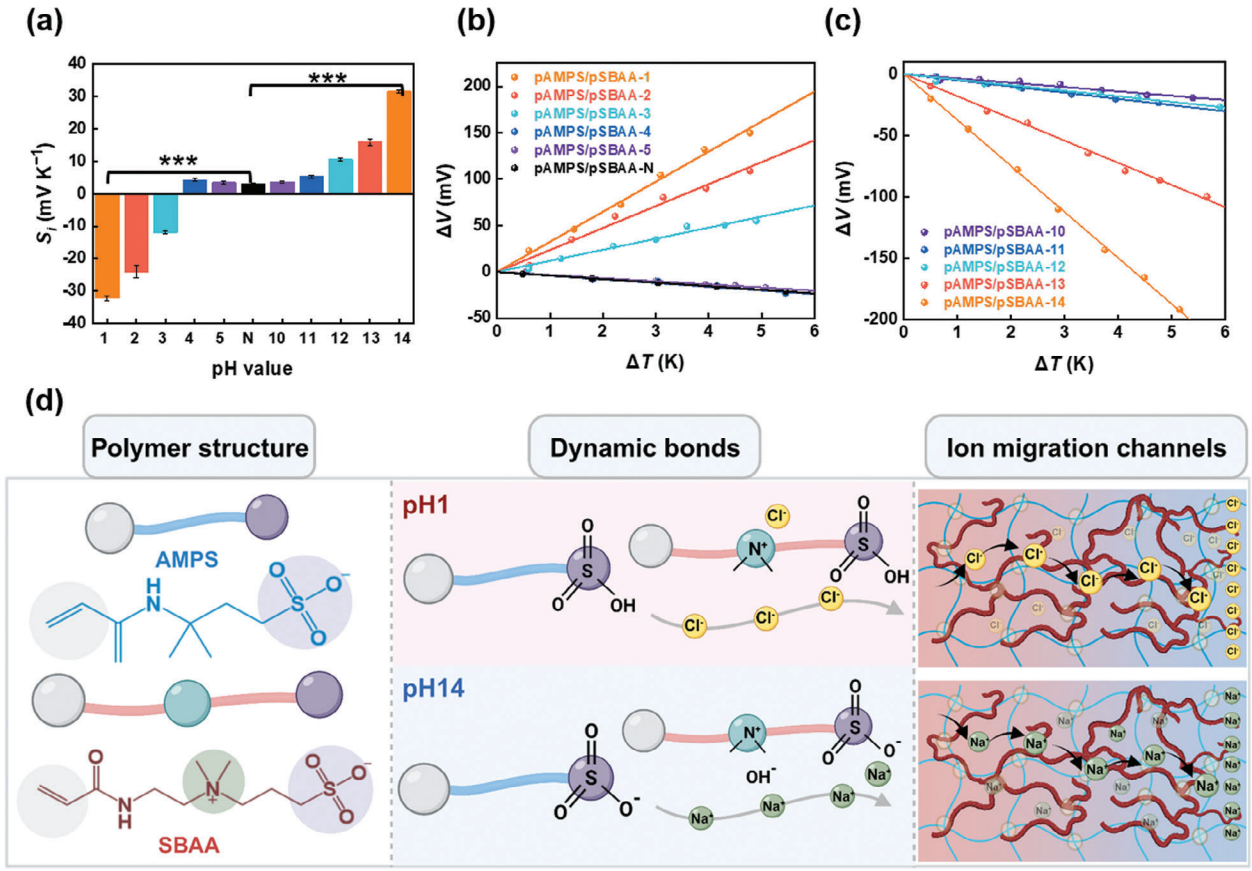

Figure 5. Thermoelectric properties of pAMPS/pSBAA-N in varied pH solutions, demonstrating an increase in ΔV of the hydrogel as a function of ΔT between the hot and cold electrodes: a) Bar chart depicting the S_i in pH 1 to 14 solutions ($n = 5$), b) in pH 1 to 5 solutions, c) in pH 10 to 14 solutions. d) Schematic illustration eluciting interatomic interactions between ions and polymers in pH 1 and 14 environments, respectively. Each data point represents the mean ± SD. The *p*-value was determined by Student's two-tailed *t*-test and statistical significance: ***$p < 0.001$.

Supporting Information, while the behavior of the pAMPS/pSBAA-X hydrogels are depicted in Figure 5b,c. The mechanism behind the pH-dependent behavior of the pAMPS/pSBAA-X hydrogel is illustrated in Figure 5d, which indicates the important role of the N^+R_4 and SO_3^- functional groups within the hydrogel. Thus, in a low pH environment (pH 1), the reduced formation of SO_3^- groups leads to the predominance of positively charged N^+R_4 groups within the polymer segments.[16] This, in turn, facilitates the preferential transport of the Cl^- ions from the HCl solution, thus leading to the observed n-type behavior. In a high pH environment (pH 14), however, the N^+R_4 groups can interact with the OH^- ions from the NaOH solution, thus allowing the formation of negatively charged SO_3^- groups within the polymer segments. This, in turn, facilitates the transport of Na^+ ions, thus giving rise to the observed p-type behavior. The observed transition in the thermoelectric characteristics of the pAMPS/pSBAA-X hydrogels from n-type to p-type behavior at pH values of 4–5 can be explained in terms of the isoelectric point, which quantifies the surface charge of a polymer. Thus, a change in pH will induce a corresponding change in the surface charge of the hydrogel, thereby altering the Zeta potential.[23] The Zeta potential measurements in Figure S7, Supporting Information, indicate that the isoelectric point of the hydrogel appears at pH 4–5, thereby confirming that the particles bear a positive charge and exhibit n-type thermoelectric properties below pH 4, but become negatively charged and exhibit p-type thermoelectric behavior above pH 4.

The interactions between the polymer segments and ions are further demonstrated by the FTIR results in **Figure 6**a,b. Here, the characteristic FTIR peak of the R–N^+ stretching vibration in the N^+R_4 group exhibits a red shift from ≈1486 cm^{-1} for the pAMPS/pSBAA-N hydrogel to ≈1482 cm^{-1} for the pAMPS/pSBAA-1, thereby indicating significantly altered interactions between Cl^- and the polymer segments. Similarly, the peak due to the stretching vibration of the S=O bond within the SO_3^- group exhibits a redshift from ≈1046 cm^{-1} for the pAMPS/pSBAA-N to ≈1043 cm^{-1} for the pAMPS/pSBAA-14, which can be attributed to the interactions between SO_3^- and Na^+. These results confirm that adjusting the pH can weaken the interactions within the polymer, and are consistent with the abovementioned transition in thermoelectric behavior. Further evidence is provided by the XPS results in Figure 6c–f. Here, the N1s spectrum of the pAMPS/pSBAA-N (Figure 6c) is deconvoluted into two peaks at 402.2 and 399.9 eV due to the N^+R and —NH groups, respectively.[24] Notably, the N^+R_4 peak is seen to shift toward a lower binding energy of 401.35 eV for the pAMPS/pSBAA-1 (Figure 6d), which can be attributed to

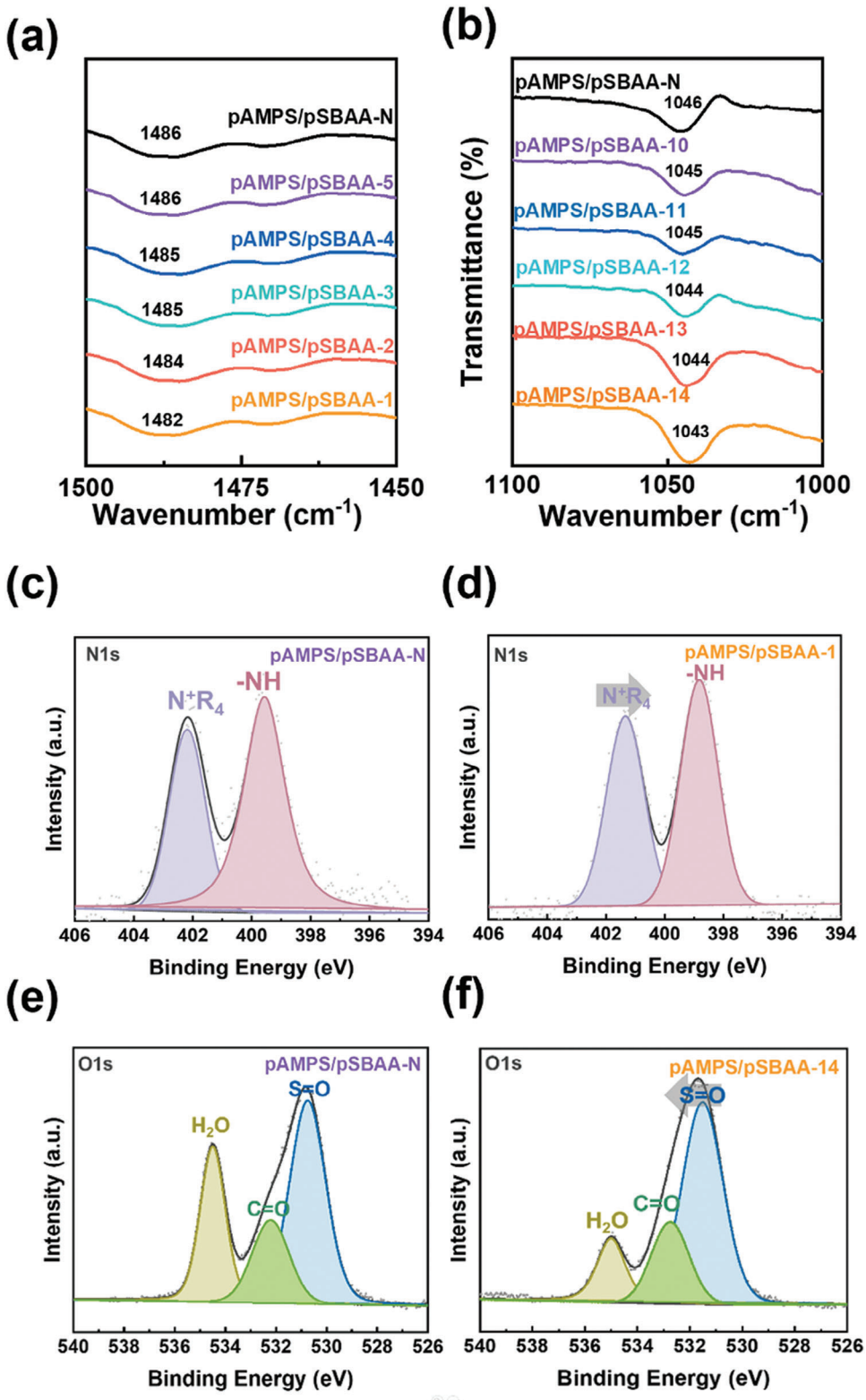

Figure 6. FTIR spectrum of pAMPS/pSBAA-N in different pH solutions: a) pAMPS/pSBAA-X at pH 1 to 5 hydrogels, b) pAMPS/pSBAA-X at pH 10 to 14 hydrogels, comparison of XPS N 1s peak: c) pAMPS/pSBAA-N hydrogels, d) pAMPS/pSBAA-1 hydrogels. Comparison of XPS O 1s peak: e) pAMPS/pSBAA-N hydrogels, f) pAMPS/pSBAA-14 hydrogels.

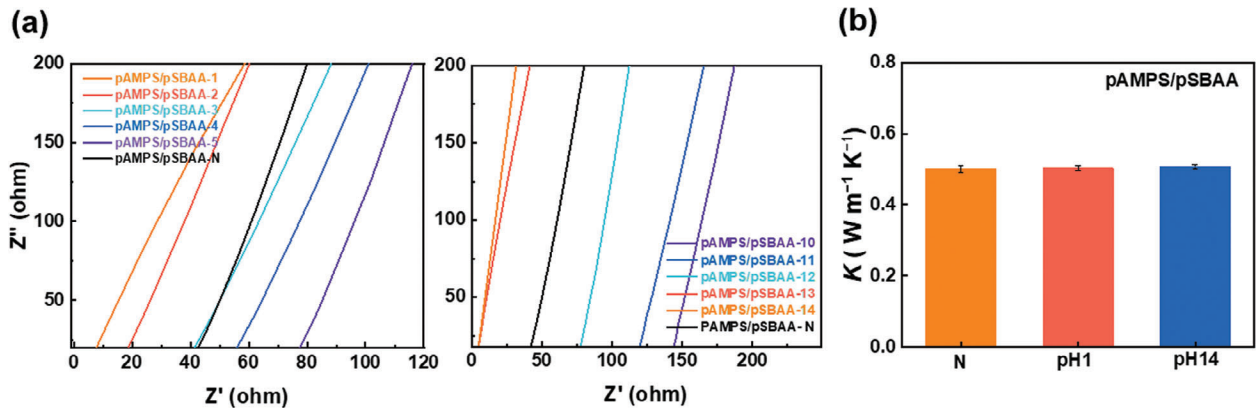

Figure 7. a) Nyquist plot of electrochemical impedance spectroscopy (EIS) for determining σ_i of pAMPS/pSBAA-X in different pH solutions. b) κ of pAMPS/pSBAA-N, pAMPS/pSBAA-1 and pAMPS/pSBAA-14.

the interaction between N^+R_4 and Cl^-. Similar changes are observed in the O 1s spectra (Figure 6e,f). Thus, the O 1s spectrum of the pAMPS/pSBAA-N (Figure 6e) is deconvoluted into three peaks at 530.7, 532.3, and 534.8 eV due to S═O, C═O, and H_2O, respectively.[25] Meanwhile, similar peaks are observed for the pAMPS/pSBAA-14 (Figure 6f), but the S═O peak is shifted toward a higher binding energy of 531.5 eV. This can be attributed to the interactions between the S═O group and the Na^+ ions. These results are consistent with previous reports.[26]

The important parameters for the i-TE properties of the hydrogels at various pH values are demonstrated in **Figure 7**a,b, and are summarized in **Table 2**. For instance, the ionic conductivity (σ_i) values of the various hydrogels are revealed by the AC impedance spectroscopy results in Figure 7a. Here, both the pAMPS/pSBAA-1 and pAMPS/pSBAA-14 exhibit notable σ_i values of around 60 mS cm^{-1}. Meanwhile, the thermal conductivity (κ) is shown in Figure 7b, where all of the pAMPS/pSBAA-X hydrogels exhibit similar values of ≈0.5 W m^{-1} K^{-1}. Based on these results, the thermoelectric performance is further evaluated by the dimensionless figure of merit (ZT_i), which is calculated using Equation (3)

$$ZT_i = \frac{\sigma_i S_i^2 T}{K} \quad (3)$$

where T is the absolute temperature. Thus, the pAMPS/pSBAA-1 hydrogel is characterized as n-type, and displays excellent i-TE characteristics, with a ZT_i value of 3.8 (Table 2). Meanwhile, the pAMPS/pSBAA-14 exhibits p-type behavior and also showcases remarkable thermoelectric properties, with a ZT_i value of 3.6.

To demonstrate this application, the pAMPS/pSBAA-1 and pAMPS/pSBAA-14 hydrogels were incorporated into ITESC devices, as shown schematically in **Figure 8**. As shown in Figure 8a, the voltage profile of the pAMPS/pSBAA-1 hydrogel during one thermal cycle can be divided into four distinct stages, which is consistent with previous studies on ZI hydrogels.[6o] Thus, during stage I, when a ΔT of 4 K is applied across the two electrodes of the ITESC, Cl^- anions accumulate on the cold side. After 9 min, this results in a ΔV of 130 mV. During stage II, upon connecting an external load of 60 kΩ to the device, the ΔV rapidly decreases due to charge screening via the external circuit. As shown in Figure 8b, the voltage decay during this stage decreases with the increase in external resistance, thus leading to an extended decay time. In stage III, when the external load is disconnected, a negative open-circuit voltage arises. As the ΔT dissipates, the accumulated cations and anions retreat into the hydrogel, while the electrons and holes necessary for charge balance remain at the two electrodes, thus leading to a

Table 2. i-TE properties of pAMPS/pSBAA hydrogels in various pH solutions.

Sample	S_i [mV K^{-1}]	σ_i [mS cm^{-1}]	κ [W m^{-1} K^{-1}]	ZT_i [–]
pAMPS/pSBAA-1[a)]	−32.6 ± 0.79	60 ± 1.03	0.5 ± 0.006	3.8 ± 0.25
pAMPS/pSBAA-2[a)]	−24.2 ± 1.87	10 ± 0.91	–	–
pAMPS/pSBAA-3[a)]	−12.4 ± 0.43	4 ± 0.23	–	–
pAMPS/pSBAA-4[b)]	4 ± 0.31	2 ± 0.52	–	–
pAMPS/pSBAA-5[b)]	3.4 ± 0.39	1.5 ± 0.51	–	–
pAMPS/pSBAA-N[b)]	3 ± 0.2	4.5 ± 0.64	0.5 ± 0.01	0.002 ± 0.001
pAMPS/pSBAA-10[b)]	3.5 ± 0.2	3 ± 0.93	–	–
pAMPS/pSBAA-11[b)]	5.1 ± 0.41	1 ± 0.13	–	–
pAMPS/pSBAA-12[b)]	10.5 ± 0.39	1.6 ± 0.35	–	–
pAMPS/pSBAA-13[b)]	16.4 ± 1.05	33 ± 0.54	–	–
pAMPS/pSBAA-14[b)]	31.7 ± 0.39	60 ± 1.12	0.5 ± 0.006	3.6 ± 0.01

[a)] n-type and [b)] p-type thermoelectric characteristics.

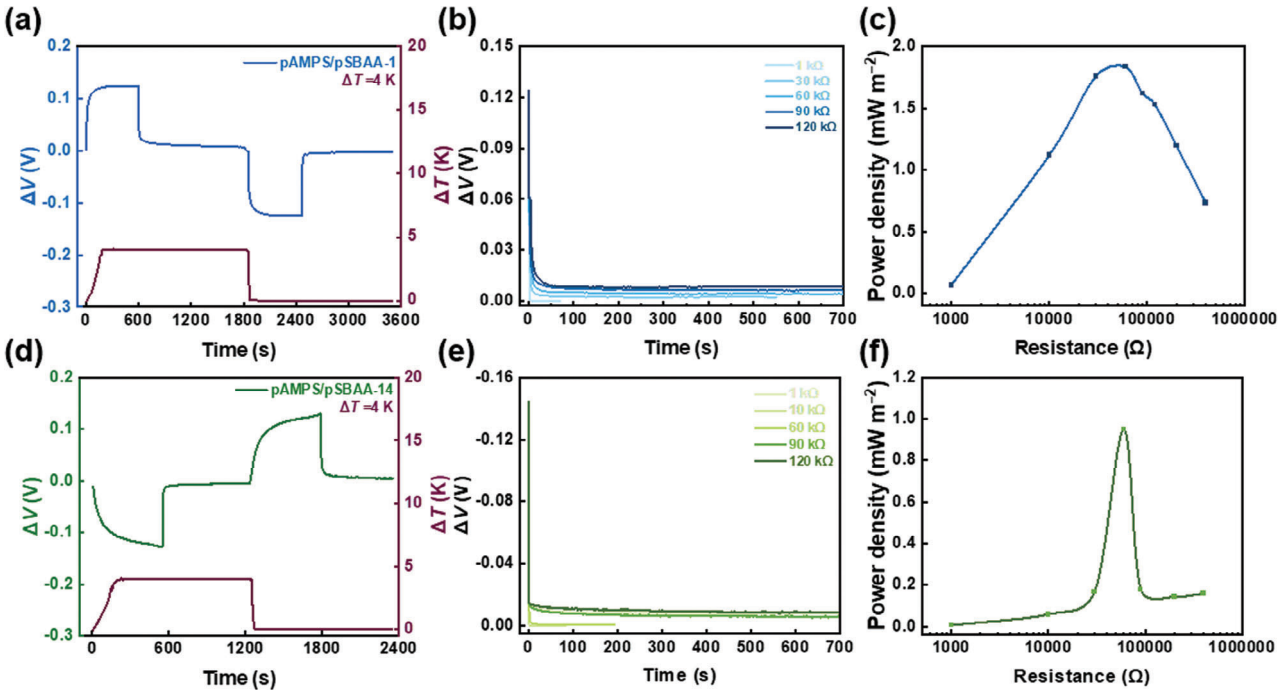

Figure 8. Performance characterization of pAMPS/pSBAA-1 and pAMPS/pSBAA-14 ITESCs. For pAMPS/pSBAA-1: a) Variations in ΔV and ΔT throughout the four-stage profile (with ΔT of 4 K), b) decay curves of ΔV on external loads with varying resistances connected to the ITESC, c) average power density supplied by the ITESCs during stage II and stage IV at the different resistances of the external load. For pAMPS/pSBAA-14: d) Variations in ΔV and ΔT throughout the four-stage profile (with ΔT of 4 K), e) decay curves of ΔV on external loads with varying resistances connected to the ITESC, f) average power density supplied by the ITESCs during stage II and stage IV at the different resistances of the external load.

corresponding change in the ΔV of approximately −130 mV. In stage IV, upon reconnecting the external load, the previously generated ΔV drops to nearly zero, corresponding to the discharge of the ITESC. The voltage profile of the pAMPS/pSBAA-14 hydrogel is depicted in Figure 8d, and the result is consistent with that of the pAMPS/pSBAA-1. Various tests were conducted on the as-fabricated ITESCs, and the average power density of the external load was calculated by using Equation (4)

$$P = E/\Delta t \tag{4}$$

where E is the energy density. This, in turn, is calculated using Equation (5)

$$E = \int V^2 \mathrm{d}t/AR \tag{5}$$

where V is the voltage across the external load, R is the resistance, A is the cross-sectional area of the electrode, dt is the charging time, and Δt is the total duration of stage II in one thermal cycle. The power densities of the as-fabricated ITESC devices under various external loads are indicated in Figure 8c.[6m] These results indicate that the maximum average power densities are obtained at an optimal external resistance of around 60 kΩ. Thus, the maximum average power density of the n-type pAMPS/pSBAA-1 hydrogel-based ITESC device is 1.8 mW m^{-2} at 60 kΩ, while that of the p-type pAMPS/pSBAA-14 hydrogel-based device is 0.9 mW m^{-2} under the same external load (Figure 8f).

Finally, the potential application of the as-fabricated hydrogel as a wearable pH sensor is demonstrated in **Figure 9**. The device uses foam nickel electrodes for the hot and cold sides, with the hydrogel securely positioned in between. A 2 × 2 mm^2 orifice is created in the foam nickel on the cold side to facilitate the introduction of acidic solutions. The theoretical voltages can be calculated by S_i (pAMPS/pSBAA-X) multiplying the ΔT. By judging from the ΔV, the pH value of hydrogels can be detected. As shown in Figure 9, after adding an acidic solution (pH 1) and maintaining a ΔT of 6 °C for 10 min, the ΔV is seen to have increased to 162.2 mV (ideal ΔV: 195.6 mV). The slight decrease in ΔV may be attributed to electrode and skin interaction, or the use of different types of electrodes. However, despite this deviation, the performance remains comparable to that of previously reported polymer-based ITESC devices.[27]

The present work offers a straightforward method for producing wearable pH-sensing and thermoelectric devices, which hold great potential for further development. Wearable pH sensors enable real-time pH level monitoring, providing insights into physiology and the environment, and aiding in health condition diagnosis. Their development promises advancements in healthcare, environmental monitoring, and scientific research.

3. Conclusion

Herein, a pH-responsive double-network hydrogel was fabricated from the negatively charged AMPS and the ZI SBAA. Due to its compact structural configuration, the as-fabricated pAMPS/pSBAA-N hydrogel displayed excellent mechanical

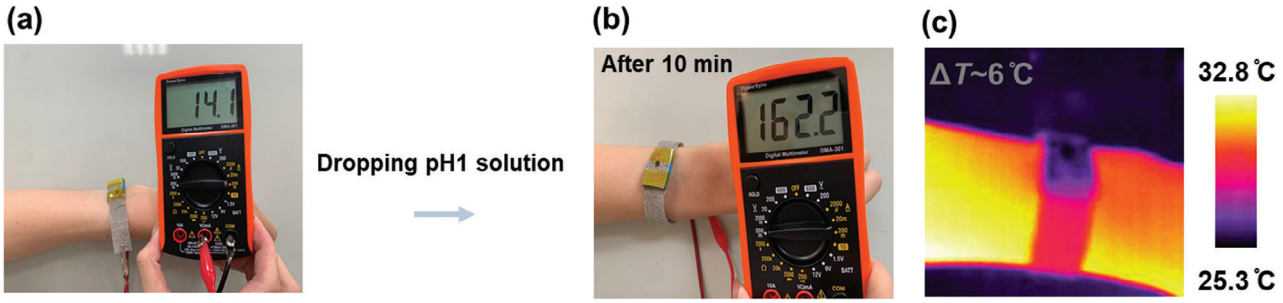

Figure 9. a) Illustration of the wearable device positioned on the wrist, accompanied by the thermal voltage resulting from the temperature difference between the human skin and the ambient environment ($\Delta T \approx 6$ °C). b) Dropping of a pH 1 solution into the device orifice after 10 min. c) Thermal image depicting the temperature distribution across the pAMPS/pSBAA-1 wearable device.

properties, including a tensile strength of 470.3 kPa and an elongation at breaking point of 106.6%. Furthermore, the pH-dependent thermoelectric behavior of the hydrogel was indicated by ionic Seebeck coefficients of −32.6 and +31.7 mV K^{-1} at pH 1 and 14, thereby indicating n-type and p-type behavior, respectively. The switch from p-type to n-type behavior occurred at around pH 4–5, and this was consistent with the isoelectric point of the hydrogel, as determined by zeta potential measurements. After immersion in acidic (pH 1) and alkaline (pH14) solutions, both the n-type pAMPS/pSBAA-1 and the p-type pAMPS/pSBAA-14 hydrogels exhibited remarkable ionic conductivity of ≈60 mS cm^{-1} along with outstanding thermoelectric characteristics, as reflected by their power density values 1.8 and 0.9 mW m^{-2}, along with figure-of-merit (ZT_i) values of 3.8 and 3.6, respectively. Finally, potential applications of these pH-responsive hydrogels in ITESCs and wearable pH sensing devices were demonstrated. This work underscores the promise of these innovative ZI hydrogels, offering facile modulation of the ZI properties and affording bipolar thermoelectric properties suitable for a wide range of energy-related applications.

4. Experimental Section

Synthesis of the pAMPS/pSBAA-N ZI Double Network Hydrogels: The synthesis of the pAMPS/pSBAA-N double network hydrogels followed a previously established protocol.[28] In brief, a precursor solution was prepared by dissolving 1 M of AMPS monomer, 4 mol% MBAA, and 0.1 mol% 2-OA in 10 mL of deionized water. This precursor solution was subjected to nitrogen degassing in the absence of light for a duration of 10 min. Subsequently, the degassed solution was cast into a mold, which was constructed using two glass plates separated by spacers. This mold yielded hydrogel sheets with variable thickness, ranging from 0.5 to 3 mm. The entire assembly was then exposed to UV-LED light ($\lambda = 365$ nm, 100 mW cm^{-2}) for a duration of 20 min under a nitrogen-protected environment. Following this photocrosslinking step, the resulting AMPS hydrogels were extracted from the mold and immersed in an SBAA monomer solution. This SBAA monomer solution was composed of a 4 M SBAA monomer, 0.02 mol% MBAA, and 0.01 mol% 2-OA. The immersion was conducted under complete darkness for a period of 3 days. After the swelling of the pAMPS hydrogels in the SBAA monomer solution, they were placed between two glass plates and subsequently exposed to UV-LED light (in a nitrogen environment for 20 min). Upon removal from the glass plates, the resulting double network hydrogels were immersed in deionized water for a duration of 3 days, with regular replacement of the water every 12 h. For the preparation of the pAMPS and pSBAA hydrogels, the same formulation as described above was used. However, these single-network hydrogels did not undergo the second polymerization step. In this study, it is important to note that pAMPS/pSBAA-N denotes the nomenclature for the ZI (interpenetrating network) hydrogel, whereas pSBAA and pAMPS represent single-network hydrogels.

Fabrication and Measurement of the ITESC: The polyelectrolytes for the ITESCs were prepared by immersing the pAMPS/pSBAA-N hydrogels in distinct pH solutions, utilizing deionized water as the solvent. A pH range spanning from ≈1 to 14 was established through the addition of either hydrochloric acid (HCl) or sodium hydroxide (NaOH). Multiple immersions were carried out to ensure complete solute replacement until the pH of the hydrogel matched that of the target solution. This process involved continuous pH monitoring using a pH meter (Eutech AIDI-pH510). Here, the nomenclature pAMPS/pSBAA-X represents the pAMPS/pSBAA-N hydrogel immersed in solutions with varying pH values. For instance, "pAMPS/pSBAA-1" corresponds to immersion in a pH 1 solution.

The Seebeck coefficient (S_i) of the pAMPS/pSBAA hydrogel was assessed within a custom-designed experimental setup maintained at 80% relative humidity. Two platinum (Pt) electrodes, each measuring 1.5 × 1.5 cm^2, were securely affixed to the upper and lower surfaces of the two end stages of the TCCs. The temperature gradient (ΔT) across the TCCs was controlled as follows: the temperature in the hot section, regulated within the range of 25 to 30 °C, was meticulously managed using a customized temperature controller. In contrast, the temperature in the cold section was held constant at 25 °C through the use of a water bath. Temperature measurements were carried out with the placement of two thermocouples situated between the Pt electrode and the hydrogel. Data acquisition was facilitated through a specialized temperature recording system. Voltage differences under each ΔT were recorded using a Keithley 2400A sourcemeter. To determine the S_i, a linear regression analysis was performed on 5 to 6 data points. Furthermore, the S_i value for pAMPS/pSBAA-X hydrogel was calculated based on data collected from five identically fabricated devices.

Statistical Analysis: The experimental result was expressed as mean ± SD at which the SD was indicated by error bars in the figures. The samples used for the determination of S_i, σ_i, and κ at each variation of pAMPS/pSBAA-X were $n = 5$. The SD of ZT_i was determined using the propagation of error approach. All the statistical analysis was carried out using Microsoft Excel and Origin software. Each data point represents the mean ± SD. The p-value was determined by Student's two-tailed t-test and statistical significance: $^{***}p < 0.001$.

Supporting Information

Supporting Information is available from the Wiley Online Library or from the author.

Acknowledgements

C.J.H. gratefully acknowledges the funding provided by National Science and Technology Council (NSTC) in Taiwan (111-2628-E-008-003-

MY3, 111-2923-E-008-004-MY3, and 112-2221-E-008-007-MY3). C.L.L. acknowledges the financial support from the 2030 Cross–Generation Young Scholars Program by NSTC in Taiwan under grants 111–2628–E–002–014 and 112–2628–E–002–013 and Academic Research–Career Development Project (Sprout Research Projects) by National Taiwan University (NTU112L7856). This work was also financially supported by the "Advanced Research Center for Green Materials Science and Technology" from The Featured Area Research Center Program within the framework of the Higher Education Sprout Project by the Ministry of Education (112L9006). The beamline BL23A1 of Taiwan Light Source (TLS) and BL13A1 of Taiwan Photon Source (TPS) from the National Synchrotron Radiation Research Center (NSRRC) of Taiwan for providing beamtime is also appreciated.

Conflict of Interest

The authors declare no conflict of interest.

Data Availability Statement

The data that support the findings of this study are available from the corresponding author upon reasonable request.

Keywords

hydrogel, ionic Seebeck coefficient, ionic thermoelectrics, low-grade heat harvesting, zwitterionic polymer

Received: December 18, 2023
Revised: February 5, 2024
Published online: February 19, 2024

[1] F. Brahman, M. Honarmand, S. Jadid, *Energy Build.* **2015**, *90*, 65.
[2] M. Papapetrou, G. Kosmadakis, A. Cipollina, U. L. Commare, G. Micale, *Appl. Therm. Eng.* **2018**, *138*, 207.
[3] a) B. Chen, Q. Chen, S. Xiao, J. Feng, X. Zhang, T. Wang, *Sci. Adv.* **2021**, *7*, eabi7233; b) Z. Li, J. Fu, X. Zhou, S. Gui, L. Wei, H. Yang, H. Li, X. Guo, *Adv. Sci.* **2023**, *10*, 2201718; c) M. Massetti, F. Jiao, A. J. Ferguson, D. Zhao, K. Wijeratne, A. Würger, J. L. Blackburn, X. Crispin, S. Fabiano, *Chem. Rev.* **2021**, *121*, 12465; d) H. Wu, X.-l. Shi, J. Duan, Q. Liu, Z.-G. Chen, *Energy Environ. Sci.* **2023**, *16*, 1870; e) L. Zhang, X.-L. Shi, Y.-L. Yang, Z.-G. Chen, *Mater. Today* **2021**, *46*, 62.
[4] a) I. H. Eryilmaz, Y.-F. Chen, G. Mattana, E. Orgiu, *Chem. Commun.* **2023**, *59*, 3160; b) Z. Soleimani, S. Zoras, B. Ceranic, Y. Cui, S. Shahzad, *Nano Energy* **2021**, *89*, 106325; c) T. Sun, L. Wang, W. Jiang, *Mater. Today* **2022**, *57*, 121.
[5] a) Z. Cao, R. Momen, S. Tao, D. Xiong, Z. Song, X. Xiao, W. Deng, H. Hou, S. Yasar, S. Altin, *Nano-Micro Lett.* **2022**, *14*, 181; b) H. Cheng, Q. Le, Z. Liu, Q. Qian, Y. Zhao, J. Ouyang, *J. Mater. Chem. C* **2022**, *10*, 433; c) M. Dupont, D. MacFarlane, J. Pringle, *Chem. Commun.* **2017**, *53*, 6288; d) B. Lei, S. Bai, S. Ju, C. Yin, C. Chen, J. Zhang, *Mater. Res. Express* **2021**, *8*, 062001; e) W. Liu, X. Qian, C.-G. Han, Q. Li, G. Chen, *Appl. Phys. Lett.* **2021**, *118*, 020501; f) Y. Liu, M. Cui, W. Ling, L. Cheng, H. Lei, W. Li, Y. Huang, *Energy Environ. Sci.* **2022**, *15*, 3670; g) Y. Liu, H. Wang, P. C. Sherrell, L. Liu, Y. Wang, J. Chen, *Adv. Sci.* **2021**, *8*, 2100669; h) Y. H. Pai, J. Tang, Y. Zhao, Z. Liang, *Adv. Energy Mater.* **2023**, *13*, 2202507; i) X. Shi, L. Ma, Y. Li, Z. Shi, Q. Wei, G. Ma, W. Zhang, Y. Guo, P. Wu, Z. Hu, *Adv. Funct. Mater.* **2023**, *33*, 2211720; j) Y. Tian, X. Yang, K. Li, Q. Zhang, Y. Li, H. Wang, C. Hou, *Mater. Today Energy* **2023**, *36*, 101342; k) W. Wang, H. Tian, D. Huo, G. Shu, *Chem. Eng. J.* **2023**, *474*, 145503; l) X. Wu, N. Gao, H. Jia, Y. Wang, *Chem. Asian J.* **2021**, *16*, 129; m) B. Yang, G. Portale, *Colloid Polym. Sci.* **2021**, *299*, 465; n) D. Zhao, A. Würger, X. Crispin, *J. Energy Chem.* **2021**, *61*, 88.
[6] a) Z. A. Akbar, J.-W. Jeon, S.-Y. Jang, *Energy Environ. Sci.* **2020**, *13*, 2915; b) Q. Chen, B. Chen, S. Xiao, J. Feng, J. Yang, Q. Yue, X. Zhang, T. Wang, *ACS Appl. Mater. Interfaces* **2022**, *14*, 19304; c) Q. Chen, B. Cheng, Z. Wang, X. Sun, Y. Liu, H. Sun, J. Li, L. Chen, X. Zhu, L. Huang, *J. Mater. Chem. A* **2023**, *11*, 2145; d) H. Cheng, J. Ouyang, *Adv. Energy Mater.* **2020**, *10*, 2001633; e) C. Chi, M. An, X. Qi, Y. Li, R. Zhang, G. Liu, C. Lin, H. Huang, H. Dang, B. Demir, *Nat. Commun.* **2022**, *13*, 221; f) C.-G. Han, X. Qian, Q. Li, B. Deng, Y. Zhu, Z. Han, W. Zhang, W. Wang, S.-P. Feng, G. Chen, *Science* **2020**, *368*, 1091; g) Y. Han, H. Wei, Y. Du, Z. Li, S. P. Feng, B. Huang, D. Xu, *Adv. Sci.* **2023**, *10*, 2302685; h) Y.-C. Hsiao, L.-C. Lee, Y.-T. Lin, S.-H. Hong, K.-C. Wang, S.-H. Tung, C.-L. Liu, *Mater. Today Energy* **2023**, *37*, 101383; i) Q. Le, H. Cheng, J. Ouyang, *Chem. Eng. J.* **2023**, *469*, 143828; j) C. Liu, Q. Li, S. Wang, W. Liu, N. X. Fang, S.-P. Feng, *Nano Energy* **2022**, *92*, 106738; k) K. Liu, J. Lv, G. Fan, B. Wang, Z. Mao, X. Sui, X. Feng, *Adv. Funct. Mater.* **2022**, *32*, 2107105; l) S. Liu, Y. Yang, H. Huang, J. Zheng, G. Liu, T. H. To, B. Huang, *Sci. Adv.* **2022**, *8*, eabj3019; m) Z. Liu, H. Cheng, Q. Le, R. Chen, J. Li, J. Ouyang, *Adv. Energy Mater.* **2022**, *12*, 2200858; n) S. Park, B. Kim, C. Cho, E. Kim, *J. Mater. Chem. A* **2022**, *10*, 13958; o) D. Zhao, H. Wang, Z. U. Khan, J. Chen, R. Gabrielsson, M. P. Jonsson, M. Berggren, X. Crispin, *Energy Environ. Sci.* **2016**, *9*, 1450.
[7] D. H. Ho, Y. M. Kim, U. J. Kim, K. S. Yu, J. H. Kwon, H. C. Moon, J. H. Cho, *Adv. Energy Mater.* **2023**, *13*, 2301133.
[8] H. Cheng, J. Ouyang, *J. Phys. Chem. Lett.* **2022**, *13*, 10830.
[9] X. Lin, X. Zhao, C. Xu, L. Wang, Y. Xia, *J. Polym. Sci.* **2022**, *60*, 2525.
[10] a) D. Dong, C. Tsao, H.-C. Hung, F. Yao, C. Tang, L. Niu, J. Ma, J. MacArthur, A. Sinclair, K. Wu, *Sci. Adv.* **2021**, *7*, eabc5442; b) S. Y. Zheng, S. Mao, J. Yuan, S. Wang, X. He, X. Zhang, C. Du, D. Zhang, Z. L. Wu, J. Yang, *Chem. Mater.* **2021**, *33*, 8418.
[11] S. Aleid, M. Wu, R. Li, W. Wang, C. Zhang, L. Zhang, P. Wang, *ACS Mater. Lett.* **2022**, *4*, 511.
[12] M. N. Moghadam, D. P. Pioletti, *J. Mech. Behav. Biomed. Mater.* **2015**, *41*, 161.
[13] C. Norioka, Y. Inamoto, C. Hajime, A. Kawamura, T. Miyata, *NPG Asia Mater* **2021**, *13*, 34.
[14] a) M. Liao, P. Wan, J. Wen, M. Gong, X. Wu, Y. Wang, R. Shi, L. Zhang, *Adv. Funct. Mater.* **2017**, *27*, 1703852; b) X. Zhu, K. Wang, Y. Xu, G. Zhang, S. Li, C. Li, X. Zhang, X. Sun, X. Ge, Y. Ma, *Energy Storage Mater.* **2021**, *36*, 291.
[15] A. I. Van Den Bulcke, B. Bogdanov, N. De Rooze, E. H. Schacht, M. Cornelissen, H. Berghmans, *Biomacromolecules* **2000**, *1*, 31.
[16] K. Qu, Z. Yuan, Y. Wang, Z. Song, X. Gong, Y. Zhao, Q. Mu, Q. Zhan, W. Xu, L. Wang, *ChemPhysMater* **2022**, *1*, 294.
[17] G. Beaucage, *J. Appl. Crystallogr.* **1995**, *28*, 717.
[18] G. Beaucage, *J. Appl. Crystallogr.* **1996**, *29*, 134.
[19] S. Sakurai, *Polym. Int.* **2017**, *66*, 237.
[20] a) Y.-C. Lin, C.-Y. Chen, H.-L. Chen, T. Hashimoto, S.-A. Chen, Y.-C. Li, *J. Chem. Phys.* **2015**, *142*, 214905; b) O. A. Shilova, *J. Sol-Gel Sci. Technol.* **2020**, *95*, 599.
[21] P. Zarrintaj, M. Jouyandeh, M. R. Ganjali, B. S. Hadavand, M. Mozafari, S. S. Sheiko, M. Vatankhah-Varnoosfaderani, T. J. Gutiérrez, M. R. Saeb, *Eur. Polym. J.* **2019**, *117*, 402.
[22] Y. He, Q. Zhang, H. Cheng, Y. Liu, Y. Shu, Y. Geng, Y. Zheng, B. Qin, Y. Zhou, S. Chen, *J. Phys. Chem. Lett.* **2022**, *13*, 4621.
[23] K. Goudie, S. McCreath, J. Parkinson, C. Davidson, J. Liggat, *J. Polym. Sci.* **2023**, *61*, 2316.
[24] R. Lapuente, C. Quijada, F. Huerta, F. Cases, J. L. Vázquez, *Polym. J.* **2003**, *35*, 911.

[25] S. Yamamoto, H. Bluhm, K. Andersson, G. Ketteler, H. Ogasawara, M. Salmeron, A. Nilsson, *J. Phys.: Condens. Matter* **2008**, *20*, 184025.
[26] G. Greczynski, L. Hultman, *Prog. Mater. Sci.* **2020**, *107*, 100591.
[27] S. Sun, M. Li, X. L. Shi, Z. G. Chen, *Adv. Energy Mater.* **2023**, *13*, 2203692.
[28] K.-T. Huang, P.-S. Hsieh, L.-G. Dai, C.-J. Huang, *J. Mater. Chem. B* **2020**, *8*, 7390.